

Bayesian Regularization for Functional Graphical Models

Jiajing Niu* Boyoung Hur* John Absher†
D. Andrew Brown‡

for the Alzheimer’s Disease Neuroimaging Initiative§

October 13, 2021

Abstract

Graphical models, used to express conditional dependence between random variables observed at various nodes, are used extensively in many fields such as genetics, neuroscience, and social network analysis. While most current statistical methods for estimating graphical models focus on scalar data, there is interest in estimating analogous dependence structures when the data observed at each node are functional, such as signals or images. In this paper, we propose a fully Bayesian regularization scheme for estimating functional graphical models. We first consider a direct Bayesian analog of the functional graphical lasso proposed by Qiao et al. (2019). We then propose a regularization strategy via the graphical horseshoe. We compare these approaches via simulation study and apply our proposed functional graphical horseshoe to two motivating applications, electroencephalography data for comparing brain activation between an alcoholic group and controls, as well as changes in structural connectivity in the presence of traumatic brain injury (TBI). Our results yield insight into how the brain attempts to compensate for disconnected networks after injury.

Key Words: Functional principal components analysis, Gaussian graphical model, horseshoe prior, structural connectivity, traumatic brain injury

*School of Mathematical and Statistical Sciences, Clemson University, Clemson, SC 29634, USA

†Prisma Health, Greenville, SC, 29605

‡Corresponding Author, School of Mathematical and Statistical Sciences, Clemson University, Clemson, SC 29634

§Data used in preparation of this article were obtained from the Alzheimer’s Disease Neuroimaging Initiative (ADNI) database (adni.loni.usc.edu). As such, the investigators within the ADNI contributed to the design and implementation of ADNI and/or provided data but did not participate in analysis or writing of this report. A complete listing of ADNI investigators can be found at: http://adni.loni.usc.edu/wp-content/uploads/how_to_apply/ADNI_Acknowledgement_List.pdf

1 Introduction

Graphical models use graphs to model and draw inferences concerning conditional independence among a collection of random variables or processes, each of which is associated with a particular location (also called a node or a vertex). They have been used to study flow cytometry between cell proteins (Friedman et al., 2008), to estimate networks from gene expression data (Li et al., 2019), and to identify communicating regions from electroencephalography (EEG) data (Qiao et al., 2019). In this work we are focused on *Gaussian* graphical models, where the data follow a multivariate Gaussian distribution. In this case estimating the edge set is equivalent to identifying the nonzero elements of the precision matrix associated with the Gaussian distribution.

Broadly speaking, frequentist studies of graphical models have either involved neighborhood selection (Meinshausen et al., 2006) or the graphical lasso (Yuan and Lin, 2007; Friedman et al., 2008). The neighborhood selection method employs regression of each variable on the remaining variables with regularization, and then summarizing the neighborhoods together. But this method can be computationally intensive and thus not scalable to larger graphs. On the other hand, Friedman et al. (2008) proposed the graphical lasso via a Gaussian log-likelihood with the lasso regularization on the entire precision matrix. The glasso has proven to be useful and is a widely used procedure, due to the sparsity and convergence rates that have been studied (Lam and Fan, 2009) as well as associated computational techniques (Friedman et al., 2008; Zhu et al., 2014). A Bayesian version of the graphical lasso was proposed by Wang (2012), who illustrated potential differences between the posterior mean and the posterior mode that might be encountered. Li et al. (2019) extended the ideas of Wang (2012) by proposing a graphical horseshoe estimator, along with an efficient Markov chain Monte Carlo (MCMC; Gelfand and Smith, 1990) algorithm for its implementation.

To date, most of the graphical modeling literature has focused on data in which each node has an associated scalar or vector-valued response variable. However, many real world applications involve the collection of functional data at each node. In this case, we have a collection of subjects / units for whom a set of continuously-supported random functions are (discretely) observed, one function at each node, where the support may be time- or spatially-indexed, or both. For example, in neuroscience there is much interest in studying connectivity; e.g., in terms of connected regions of interest measured in functional magnetic resonance imaging (fMRI; Shappell et al., 2019) or communicating electrodes in electroencephalography (EEG; Zhang et al., 1995) corresponding to associated regions of neuronal activity. Alternatively, in social network analysis and marketing, it is possible to observe and record online behavior patterns among baskets of different goods for each customer over a period of time to identify related types of products. Compared to scalar or vector-valued graphical models, functional graphical models remain vastly underexplored. Qiao et al. (2019) proposed a functional version of the graphical lasso along with a block-coordinate descent algorithm for optimizing the loss function. Around the same time, Zhu et al. (2016) proposed a Bayesian framework for working with functional graphical models directly in the space of infinite-dimensional random functions, essentially extending the work of Dawid and Lauritzen (1993) to function space by using hyper-inverse Wishart priors to a priori model the space of plausible, decomposable graphs. Recently, Zhang et al. (2021) proposed a Bayesian model for functional graphical models in which independent Laplace priors are

placed on reparameterized partial correlations associated with basis coefficients, inducing a so-called normal hypo-exponential shrinkage prior and allowing the graph to functionally evolve over time. To the best of our knowledge, Zhu et al. (2016) and Zhang et al. (2021) are the only works on Bayesian functional graphical models.

Our work is motivated by neuroimaging data that typically have low signal-to-noise ratios caused by non-neural noise arising from cardiac and respiratory processes or scanner instability, a problem that is exacerbated by the typically small numbers of subjects available from such studies. For instance, in Section 5.2 we study the effects of traumatic brain injury on connectivity of the human brain. The diffusion-weighted magnetic resonance imaging data consist of longitudinal measurements of white matter integrity within 26 regions of interest in 34 subjects, 17 of whom have been diagnosed with a traumatic brain injury (TBI). We aim to assess chronic structural connectivity differences between the TBI and non-TBI groups using the sparse, irregularly-measured longitudinal data — a goal for which few techniques currently exist. Further, quantifying model uncertainty is important. For example, Greenlaw et al. (2017) used an imaging genetics example to demonstrate dramatic differences in associations between genetic variations and brain imaging measures that might be identified when accounting for uncertainty in a model estimate versus using an optimization-based point estimate alone.

In this paper, we propose two different regularization schemes for functional graphical models. The first approach we consider is a direct Bayesian version of the frequentist functional graphical lasso proposed by Qiao et al. (2019). We propose also a functional graphical horseshoe, due to the horseshoe’s known improvements upon the lasso’s tendency to over-shrink large coefficients and under-shrink small coefficients in high-dimensional problems (Wang, 2012; Li et al., 2019). Whereas most existing Bayesian approaches to covariance or precision matrix estimation assume structure such as banded covariance (e.g., Banerjee and Ghosal, 2014) or decomposable graphs (e.g., Rajaratnam et al., 2008; Xiang et al., 2015; Zhu et al., 2016), neither the Bayesian functional graphical lasso nor the functional graphical horseshoe assume any structure other than sparsity. We provide efficient Gibbs sampling algorithms for both of our proposed models, exploiting auxiliary variables to produce a set of easily-sampled conditional distributions. Through extensive simulation studies, we evaluate both the classification accuracy and fidelity of the estimated coefficients. We apply our proposed Bayesian functional graphical horseshoe to two motivating datasets, the EEG alcoholic versus control study presented by Qiao et al. (2019), and a novel study of white matter connectivity between healthy patients and those with a history of traumatic brain injury using data obtained from the Alzheimer’s Disease Neuroimaging Initiative (ADNI).

This article is organized as follows: In Section 2, we provide a brief background for Gaussian graphical models, including basic concepts and notations for structure learning through precision matrix estimation as well as the original graphical lasso (Yuan and Lin, 2007). The Section also reviews functional principal component analysis (FPCA) and its connection to both the frequentist and Bayesian regularization approaches to functional graphical models. In Section 3, we present both of our proposed approaches, the Bayesian functional graphical lasso and the functional graphical horseshoe model, as well as efficient Gibbs samplers. We present and discuss statistical and computational performance of our proposed methods in Section 4, followed by applying the functional graphical horseshoe to the motivating applications in Section 5. A summary and concluding remarks may be

found in Section 6. The code for implementing our proposed algorithms is available at <https://github.com/jjniu/BayesFGM>.

2 Background

2.1 Gaussian Graphical Models and the Graphical Lasso

Suppose the random vector $\mathbf{y} = (y_1, \dots, y_p)^T$ follows a multivariate Gaussian distribution with mean $\boldsymbol{\mu}$ and covariance matrix $\boldsymbol{\Sigma}$. Then we define $\boldsymbol{\Theta} = \boldsymbol{\Sigma}^{-1}$ as the *precision matrix*, or concentration matrix. A Gaussian graphical model (GGM) is based on an undirected graph $G = (V, E)$, where $V = \{1, \dots, p\}$ is a non-empty set of vertices and $E \subseteq \{(i, j), i < j\}$ is a set of edges representing unordered pairs of vertices (also called nodes). Each variable y_i is represented by a node in the graph, and E determines the precision matrix in that, for $i \neq j$, $(\boldsymbol{\Theta})_{ij} \neq 0$ if and only if $(i, j) \in E$. By Theorem 2.2 in Rue and Held (2005), we thus have that E encodes a Markov property in the distribution. Letting $\mathcal{N}(i) = \{j : (i, j) \in E\}$ and adopting the convention that $\mathbf{y}_{\mathcal{A}} = (y_j : j \in \mathcal{A})^T$ for a set of indices \mathcal{A} , we have that, for any node i , $y_i | \mathbf{y}_{(-i)} \stackrel{d}{=} y_i | \mathbf{y}_{\mathcal{N}(i)}$. Extending this with $V = \{1, \dots, p\}$, it follows that $y_u \perp\!\!\!\perp y_v | \mathbf{y}_{V \setminus \{u, v\}}$ if and only if $(\boldsymbol{\Theta})_{uv} = 0$, where $\perp\!\!\!\perp$ denotes statistical independence. This is the *pairwise Markov property*. By this property, learning the graph associated with a Gaussian graphical model is equivalent to estimating the precision matrix of the multivariate Gaussian distribution, making it a covariance estimation problem (Dempster, 1972).

Given a sample \mathbf{y}_i , $i = 1, \dots, n$, stored in a data matrix $\mathbf{Y} = (\mathbf{y}_1 \cdots \mathbf{y}_n)^T$, the goal is to estimate and select non-zero elements of $\boldsymbol{\Theta}$, thereby obtaining an estimate of the undirected graph associated with the GGM. The log-likelihood of $\boldsymbol{\Theta}$ (up to an additive constant) can be written as

$$l(\boldsymbol{\Theta}) = \log \det \boldsymbol{\Theta} - \text{tr}(\mathbf{S}\boldsymbol{\Theta}/n), \quad (1)$$

where $\mathbf{S} = \mathbf{Y}^T \mathbf{Y}$. The quantity $-l(\boldsymbol{\Theta})$ is a convex function of $\boldsymbol{\Theta}$ and the maximum likelihood estimator of $\boldsymbol{\Sigma}$ is $\widehat{\boldsymbol{\Sigma}} = \mathbf{S}/n$. This estimator enjoys nice properties such as consistency, but can be unstable when $p \approx n$. Further, even when $\widehat{\boldsymbol{\Sigma}}^{-1}$ exists, it can be an unsatisfactory estimator of $\boldsymbol{\Theta}$ due to the fact that it will generally not be sparse, even if $\widehat{\boldsymbol{\Sigma}}$ is sparse.

To find a more stable estimator of $\boldsymbol{\Theta}$ that is simultaneously sparse, Yuan and Lin (2007) proposed to solve a lasso-type regularized version of the likelihood objective function by finding

$$\widehat{\boldsymbol{\Theta}} = \arg \min_{\boldsymbol{\Theta} \in M^+} \{-\log \det \boldsymbol{\Theta} + \text{tr}(\mathbf{S}\boldsymbol{\Theta}/n) + \lambda \|\boldsymbol{\Theta}\|_1\}, \quad (2)$$

where M^+ is the space of $p \times p$ symmetric positive definite matrices, the norm $\|\cdot\|_1$ is the sum of the absolute values of the off-diagonal elements, and λ is a non-negative tuning parameter. Like the original lasso (Tibshirani, 1996; Knight and Fu, 2000), Yuan and Lin (2007) showed that, for a given λ value, the solution to this minimization problem produces a \sqrt{n} -consistent estimator of the true precision matrix. Yuan and Lin (2007) solved this problem with the so-called maxdet algorithm (Vandenberghe et al., 1998). However, by connecting it to earlier work on the lasso, Friedman, Hastie, and Tibshirani (2008) proposed a more efficient coordinate descent algorithm for solving (2). This is the *graphical lasso*, an approach that has since become very popular for structure learning in GGMs.

Wang (2012) considered the fully Bayesian version of the graphical lasso by recognizing that solving (2) is equivalent to finding the maximum a posteriori (MAP) estimator in the following model,

$$p(\mathbf{y}_i | \Theta) = N(\mathbf{y}_i | \mathbf{0}, \Theta^{-1}), \quad i = 1, \dots, n \quad (3)$$

$$p(\Theta | \lambda) \propto \prod_{i < j} DE(\theta_{ij} | \lambda) \prod_{i=1}^p \text{Exp}\left(\theta_{ii} | \frac{\lambda}{2}\right), \quad \Theta \in M^+, \quad (4)$$

where $N(\cdot | \mathbf{0}, \Theta^{-1})$ denotes the density of a $N(\mathbf{0}, \Theta^{-1})$ distribution, and likewise for the double exponential (DE) and exponential (Exp) distributions. Using a hierarchical representation of this model (Kyung et al., 2010) and matrix partitioning techniques similar to those employed by Banerjee et al. (2008) and Friedman et al. (2008), Wang (2012) developed an efficient Gibbs sampler for exploring the full posterior distribution and thus was able to extensively compare the results of the MAP and posterior mean estimators.

2.2 Functional Principal Component Analysis

For subject i , $i = 1, \dots, n$, let the underlying, infinite dimensional function of interest be denoted $g_i(t)$, $t \in \mathcal{T}$. We assume that g_1, \dots, g_n are identically distributed and independent zero-mean functions in $L^2[\mathcal{T}]$ with covariance function $\text{cov}(g_j(s), g_j(t)) =: \Sigma(s, t)$, $(s, t) \in \mathcal{T} \times \mathcal{T}$, where \mathcal{T} is a compact interval on the real line. Karhunen (1946) and Loeve (1963) independently discovered the functional principal component analysis (FPCA) expansion (e.g., Bosq, 2012),

$$g_i(t) = \sum_{k=1}^{\infty} a_{ik} \phi_k(t), \quad (5)$$

where $\{\phi_k(t)\}_{k=1}^{\infty}$ are the orthonormal set of eigenfunctions with corresponding eigenvalues $\{\lambda_k\}_{k=1}^{\infty}$ satisfying $\Sigma(s, t) = \sum_{k=1}^{\infty} \lambda_k \phi_k(s) \phi_k(t)$, by Mercer's Theorem, and $a_{ik} = \int g_i(t) \phi_k(t) dt$ are the functional principal component (FPC) scores of g_i , uncorrelated across k with $E(a_{ik}) = 0$ and $\text{var}(a_{ik}) = \lambda_k$. By assumption, the a_{ik} are independent across i . Like ordinary principal components analysis (e.g. Jolliffe, 2002), the expansion can be truncated to obtain a finite-dimensional approximation to the infinite-dimensional process. In what follows, the proposed functional graphical models can work with any basis expansion (e.g., wavelets or Fourier), but we use FPCA due to the mean square optimality of the truncated approximation.

Performing FPCA in practice amounts to finding the spectral decomposition of an approximation to the covariance function. When g_i , $i = 1, \dots, n$, are observed on the same evenly spaced grid t_1, \dots, t_m independent of i , this amounts to standard singular value decomposition of the sample covariance matrix. For irregularly spaced functions and/or different numbers of observations on each function, SVD will likely provide a poor approximation to the true eigensystem associated with $\Sigma(\cdot, \cdot)$. In this case, Yao et al. (2005) proposed the PACE algorithm for performing FPCA via conditional expectation. In our applications, we use SVD for the EEG example and PACE for the diffusion MRI example, as the latter involves irregularly sampled longitudinal data.

2.3 Functional Graphical Models

For a particular subject i , suppose we (discretely) observe p functions $g_{i1}(t), \dots, g_{ip}(t)$ where g_{ij} is the function observed on node j . Suppose further that each function is a Gaussian process so that (g_{i1}, \dots, g_{ip}) is a realization from a p -dimensional multivariate Gaussian process (MGP). As in typical GGMs, we associate to the MGP an undirected graph $G = (V, E)$ that represents the conditional dependence network. Here, conditional dependence of the functions g_{ij} and $g_{ij'}$ is in terms of the cross-covariance function,

$$C_{jj'}(s, t) = \text{cov}(g_{ij}(s), g_{ij'}(t) \mid g_k(\cdot), k \neq j, j'), \quad (6)$$

assumed to be the same for $i = 1, \dots, n$.

With the covariance function in hand, we can use FPCA and approximate each g_{ij} with the M -dimensional truncation,

$$g_{ij}^M(t) = \sum_{k=1}^M a_{ijk} \phi_{jk}(t), \quad M < \infty. \quad (7)$$

The function for subject i at node j can thus be represented with the coefficient vector $\mathbf{a}_{ij}^M = (a_{ij1}, \dots, a_{ijM})^T$, so that each subject's entire functional information over all p nodes is encoded in $\mathbf{a}_i^M = ((\mathbf{a}_{i1}^M)^T, \dots, (\mathbf{a}_{ip}^M)^T)^T \in \mathbb{R}^{Mp}$. Under the Gaussian assumption and independently observed subjects, the Kahrnen-Loève Theorem tells us that $\mathbf{a}_i^M \stackrel{\text{iid}}{\sim} N_{Mp}(\mathbf{0}, (\Theta^M)^{-1})$. For learning the graphical model, Qiao et al. (2019, Lemma 1) show that, in the finite-rank case (in which the M -truncated approximation is exact),

$$E^M = \{(i, j) : \|\Theta_{ij}^M\|_F \neq 0, (i, j) \in V^2, i \neq j\}, \quad (8)$$

where Θ_{ij}^M is the $M \times M$ block submatrix of Θ^M corresponding to the node pair $(i, j) \in V \times V$ and $\|\cdot\|_F$ is the Frobenius norm. Thus, structure learning in the functional graphical model is equivalent to finding the (i, j) pairs for which $\|\Theta_{ij}^M\|_F \neq 0$.

The connection in (8) to the graphical lasso and the group lasso (Yuan and Lin, 2006) led Qiao et al. (2019) to propose estimating the graph from functional data with

$$\hat{\Theta}^M = \arg \max_{\Theta^M} \left\{ \log \det \Theta^M - \text{tr}(\mathbf{S}^M \Theta^M) - \lambda_n \sum_{i \neq j} \|\Theta_{ij}^M\|_F \right\} \quad (9)$$

where \mathbf{S}^M is the sample covariance matrix computed from estimated FPC scores $\hat{\mathbf{a}}_i^M \in \mathbb{R}^{Mp}$, found via SVD or otherwise, and $\lambda_n > 0$ is a tuning parameter. As with the group lasso, blockwise sparsity is achieved as $\lambda_n \rightarrow \infty$. Qiao et al. term this approach the *functional graphical lasso* (fglasso). The edge set of the estimated graph is then $\hat{E}^M = \{(i, j) : \|\hat{\Theta}_{ij}^M\|_F \neq 0, (i, j) \in V^2, i \neq j\}$. Qiao et al. (2019) show that the fglasso enjoys model selection consistency, and provide a block coordinate descent algorithm for optimizing the objective function.

3 Bayesian Functional Graphical Models

3.1 The Bayesian Fglasso

It is well known that frequentist optimization of objective functions may often be viewed as maximum a posteriori (MAP) estimation under a Bayesian model, provided there exists a prior density corresponding to the penalty term in the objective function. For the fglasso objective function in (9), the Bayesian counterpart uses a prior on the precision matrix given by

$$\pi(\Theta) \propto \exp \left\{ -\lambda \sum_{i \neq j} \|\Theta_{ij}\|_F \right\}, \quad (10)$$

where $\|\cdot\|_F$ denotes the Frobenius norm and $\Theta_{ij} \in \mathbb{R}^{M \times M}$ is the (i, j) th submatrix in Θ associated with the conditional cross-correlation between node i and node j , $i, j = 1, \dots, p$; $i \neq j$. Since the precision matrix is symmetric, we need only to consider the upper off-diagonal elements for computational simplicity. As used in the Bayesian group lasso hierarchical representation (Kyung et al., 2010), we have the following identity,

$$\begin{aligned} \exp(-\lambda \|\Theta_{ij}\|_F) &= \int_0^\infty \left(\frac{1}{2\pi\tau_{ij}^2} \right)^{\frac{M^2}{2}} \exp \left(-\frac{\|\Theta_{ij}\|_F^2}{2\tau_{ij}^2} \right) \frac{\left(\frac{\lambda^2}{2} \right)^{\frac{M^2+1}{2}} (\tau_{ij}^2)^{\frac{M^2+1}{2}-1}}{\Gamma \left(\frac{M^2+1}{2} \right)} \\ &\quad \times \exp \left(-\frac{\lambda^2 \tau_{ij}^2}{2} \right) d\tau_{ij}^2. \end{aligned} \quad (11)$$

Thus, we can rewrite $\pi(\Theta)$ as a scale mixture of a multivariate normal distribution on the off-diagonal elements. Let $\omega_{ij} = \text{vec}(\Theta_{ij}) \in \mathbb{R}^{M^2}$, for $i, j = 1, \dots, p$, $i \neq j$. Then we can introduce the auxiliary latent parameters $\tau = (\tau_{ij})$, so the prior in (10) can be attained as a gamma mixture of normals, leading to the functional graphical lasso hierarchy

$$\omega_{ij} | \tau_{ij}^2 \sim N_{M^2}(\mathbf{0}, \tau_{ij}^2 \mathbf{I}_{M^2}); \quad \tau_{ij}^2 \sim \text{Gamma} \left(\frac{M^2 + 1}{2}, \frac{\lambda^2}{2} \right). \quad (12)$$

Denote with $\hat{\mathbf{a}}_i = (\hat{\mathbf{a}}_{i1}^T, \dots, \hat{\mathbf{a}}_{ip}^T)^T \in \mathbb{R}^{Mp}$ the estimated M -truncated functional principal component scores for the observed functions on sample i , $g_{i1}(\cdot), \dots, g_{ip}(\cdot)$, where for simplicity we assume the truncation level M is the same across all p nodes. When $(g_{i1}(\cdot), \dots, g_{ip}(\cdot))$ are drawn from an MGP, $\hat{\mathbf{a}}_i$ follows an Mp -dimensional Gaussian distribution. Then the Bayesian fglasso model can be expressed as

$$\begin{aligned} p(\hat{\mathbf{a}}_i | \Theta) &= N_{Mp}(\hat{\mathbf{a}}_i | \mathbf{0}, \Theta^{-1}), \quad i = 1, \dots, N \\ p(\Theta | \lambda) &= \frac{1}{C} \prod_{\ell=1}^{Mp} \text{Exp} \left(\theta_{\ell\ell} | \frac{\lambda^2}{2} \right) \prod_{i < j} N_{M^2}(\omega_{ij} | \mathbf{0}, \tau_{ij}^2 \mathbf{I}_{M^2}) \text{Gamma} \left(\tau_{ij}^2 | \frac{M^2 + 1}{2}, \frac{\lambda^2}{2} \right), \end{aligned} \quad (13)$$

where $\theta_{11}, \dots, \theta_{pp}$ are the diagonal elements of Θ and C is a normalizing constant.

The hierarchical representation in (12) facilitates the use of conditional conjugacy in deriving a block Gibbs sampler for exploring the posterior distribution. For a fixed regularization parameter λ , the posterior distribution associated with the Bayesian fglasso model

(13) is given by

$$\begin{aligned}
p(\Theta, \tau^2 | \mathbf{S}, \lambda) &\propto |\Theta|^{\frac{n}{2}} \exp \left\{ -\text{tr} \left(\frac{1}{2} \mathbf{S} \Theta \right) \right\} \prod_{\ell=1}^p \frac{\lambda^2}{2} \exp \left(-\frac{\lambda^2}{2} \theta_{\ell\ell} \right) \\
&\times \prod_{i < j} \left(\frac{1}{2\pi\tau_{ij}^2} \right)^{\frac{M^2}{2}} \exp \left(-\frac{\|\Theta_{ij}\|_F^2}{2\tau_{ij}^2} \right) \\
&\times \left\{ \frac{\left(\frac{\lambda^2}{2} \right)^{\frac{M^2+1}{2}} (\tau_{ij}^2)^{\frac{M^2+1}{2}-1}}{\Gamma \left(\frac{M^2+1}{2} \right)} \exp \left(-\frac{\lambda^2 \tau_{ij}^2}{2} \right) \right\} \mathbf{1}_{\Theta \in M^+},
\end{aligned} \tag{14}$$

where $\mathbf{S} = \sum_{i=1}^n \mathbf{a}_i \mathbf{a}_i^T$ is the sample scatter matrix of the functional PC scores. This representation allows us to adapt the block Gibbs sampling scheme proposed by Wang (2012).

By assumption, the off-diagonal entries of each block submatrix on the main diagonal, Θ_{ii} , $i = 1, \dots, p$, are all zeros. Partition the precision and sample fpc score covariance matrix as follows:

$$\Theta = \begin{bmatrix} \Theta_{11} & \boldsymbol{\theta}_{12} \\ \boldsymbol{\theta}_{12}^T & \theta_{22} \end{bmatrix}, \quad \mathbf{S} = \begin{bmatrix} \mathbf{S}_{11} & \mathbf{s}_{12} \\ \mathbf{s}_{12}^T & s_{22} \end{bmatrix} \tag{15}$$

where we define

$$\boldsymbol{\theta}_{12} = \begin{bmatrix} \bar{\boldsymbol{\theta}}_{12} \\ \mathbf{0} \end{bmatrix}. \tag{16}$$

With Θ permuted so that the last column / row corresponds to node j and score k , $\bar{\boldsymbol{\theta}}_{12} = \text{Cov}(a_{jk}, (\mathbf{a}_1, \dots, \mathbf{a}_{j-1}, \mathbf{a}_{j+1}, \dots, \mathbf{a}_p)^T) \in \mathbb{R}^{M(p-1)}$ with $\mathbf{a}_k \in \mathbb{R}^M$ the collection of fpc scores at node k . The $\mathbf{0} \in \mathbb{R}^{M-1}$ vector follows from a_{jk} being uncorrelated with other scores at node j .

Define $\mathbf{T} = (\tau_{ij}^2)_{p \times p} \otimes \mathbf{J}_{M \times M}$ where $\tau_{ii} = 0$ for $i = 1, \dots, p$ and $\mathbf{J}_{M \times M} = \mathbf{1}\mathbf{1}^T$ is the matrix with all ones. We similarly partition it as

$$\mathbf{T} = \begin{bmatrix} \mathbf{T}_{11} & \mathbf{t}_{12} \\ \mathbf{t}_{12}^T & 0 \end{bmatrix}, \tag{17}$$

where

$$\mathbf{t}_{12} = \begin{bmatrix} \bar{\mathbf{t}}_{12} \\ \mathbf{0} \end{bmatrix} \tag{18}$$

with $\bar{\mathbf{t}}_{12} \in \mathbb{R}^{M(p-1)}$ defined analogously to $\bar{\boldsymbol{\theta}}_{12}$.

The conditional distribution of the nonzero variables in the last column (or row) of Θ is

$$\begin{aligned}
p(\bar{\boldsymbol{\theta}}_{12}, \theta_{22} | \Theta_{11}, \mathbf{T}, \mathbf{S}, \lambda) &\propto (\theta_{22} - \bar{\boldsymbol{\theta}}_{12}^T \overline{\Theta_{11}^{-1}} \bar{\boldsymbol{\theta}}_{12})^{\frac{n}{2}} \\
&\times \exp \left\{ -\frac{1}{2} [\bar{\boldsymbol{\theta}}_{12}^T \mathbf{D}_\tau^{-1} \bar{\boldsymbol{\theta}}_{12} + 2\bar{\mathbf{s}}_{12}^T \bar{\boldsymbol{\theta}}_{12} + (s_{22} + \lambda^2)\theta_{22}] \right\}
\end{aligned} \tag{19}$$

where $\mathbf{D}_\tau = \text{diag}(\bar{\mathbf{t}}_{12})$ and $\overline{\Theta_{11}^{-1}} \in \mathbb{R}^{M(p-1) \times M(p-1)}$ is the cross covariance matrix associated with the remaining $p - 1$ nodes. We make a change of variables, $\boldsymbol{\beta} = \bar{\boldsymbol{\theta}}_{12}$, $\gamma = (\theta_{22} -$

$\bar{\boldsymbol{\theta}}_{12}^T \bar{\boldsymbol{\Theta}}_{11}^{-1} \bar{\boldsymbol{\theta}}_{12}$), and denote $\mathbf{C} = (\mathbf{D}_\tau^{-1} + (s_{22} + \lambda^2) \bar{\boldsymbol{\Theta}}_{11}^{-1})^{-1}$. This implies

$$\boldsymbol{\beta}, \gamma | \boldsymbol{\Theta}_{11}, \mathbf{T}, \mathbf{S}, \lambda \sim N_{M(p-1)}(-\mathbf{C} \bar{\mathbf{s}}_{21}, \mathbf{C}) \text{Gamma} \left(\frac{n}{2} + 1, \frac{s_{22} + \lambda^2}{2} \right). \quad (20)$$

All elements in the matrix $\boldsymbol{\Theta}$ can be sampled by sampling one row and column at a time, permuting $\boldsymbol{\Theta}$ after each iteration. Due to the structure of $\hat{\boldsymbol{\alpha}}_i$, we first cycle through all columns corresponding to the same node, then move to next node.

After complete updating of all the off-diagonal elements, the diagonal elements of $\boldsymbol{\Theta}$ and the shrinkage parameters τ_{ij} need to be sampled. The full conditional distributions of $(\tau_{ij}^2)^{-1}$ are seen to be independently inverse Gaussian with mean $\sqrt{\frac{\lambda^2}{\|\boldsymbol{\Theta}_{ij}\|_F^2}}$ and shape λ^2 . Put another way, the reparameterized model based on one particular permutation of $\boldsymbol{\Theta}$ under the Bayesian functional graphical lasso is

$$\begin{aligned} \boldsymbol{\beta} | \boldsymbol{\Theta}_{11}, \mathbf{T}, \mathbf{S}, \lambda &\sim N_{M(p-1)}(-\mathbf{C} \bar{\mathbf{s}}_{21}, \mathbf{C}) \\ \gamma | \mathbf{S}, \lambda &\sim \text{Gamma} \left(\frac{n}{2} + 1, \frac{s_{22} + \lambda^2}{2} \right) \\ \frac{1}{\tau_{ij}^2} | \boldsymbol{\Theta}_{ij}, \lambda &\stackrel{\text{indep.}}{\sim} \text{Inverse Gaussian} \left(\sqrt{\frac{\lambda^2}{\|\boldsymbol{\Theta}_{ij}\|_F^2}}, \lambda^2 \right), \quad i, j = 1, \dots, p; i \neq j. \end{aligned} \quad (21)$$

Since $\gamma > 0$ with probability one, the positive definite constraint on $\boldsymbol{\Theta}$ is maintained in each iteration. The argument for the functional case is adapted from that given by Wang (2012). Suppose at the current iteration the sample $\boldsymbol{\Theta}^{(c)}$ is positive definite, so all its pM corresponding leading principal minors are positive. After updating the particular column and row of $\boldsymbol{\Theta}$ by sampling $\boldsymbol{\beta}$ and γ by (21), the new sample $\boldsymbol{\Theta}^{(c+1)}$ has the same leading principal minors as $\boldsymbol{\Theta}^{(c)}$ except the one corresponding to the updated column/row, which is of order pM . It is easy to find that this last leading principal minor is $\det(\boldsymbol{\Theta}^{(c+1)}) = \gamma \det(\boldsymbol{\Theta}_{11}^{(c)})$, where $\det(\boldsymbol{\Theta}_{11}^{(c)})$ is the $(pM - 1)^{\text{th}}$ leading principal minor of $\boldsymbol{\Theta}^{(c)}$ excluding the updated column and row. Thus $\gamma > 0$ means that $\det(\boldsymbol{\Theta}^{(c+1)}) > 0$ and all leading principal minors of the updated matrix are positive. To ensure each MCMC realization $\boldsymbol{\Theta}^{(m)} \in M^+$ for $m = 0, 1, 2, \dots$, it is only required that the chain is initialized with $\boldsymbol{\Theta}^{(0)} \in M^+$. Algorithm 1 details the Bayesian fglasso Gibbs sampler.

Given the MCMC output of a sample of precision matrices, $\boldsymbol{\Theta}^{(1)}, \dots, \boldsymbol{\Theta}^{(L)}$, several inferential procedures are possible for constructing an estimate of $\boldsymbol{\Theta}$. Continuous shrinkage priors do not put positive probability mass on exact zeros in the precision matrix, and Carvalho et al. (2010) argue that using (non zero) posterior means as the basis for inference is often preferable to binary thresholding due to the estimator's optimality under squared error loss. Nevertheless, it is sometimes necessary to produce a sparse estimate with exact zeros, especially in the case of graphical models. Carvalho et al. (2010) and Wang (2012) discuss some possible thresholding rules. In our case, we construct the precision matrix (and thus graph) estimate $\hat{\boldsymbol{\Theta}}_{\text{thres}}$ by setting $(\hat{\boldsymbol{\Theta}}_{\text{thres}})_{kl} = 0$ if the marginal posterior credible interval contains zero. Note that different levels of sparsity may be achieved by using credible intervals at different levels.

The Bayesian fglasso proposed here assumes that the regularization parameter λ is fixed, meaning that it must be tuned and selected *a priori*. Cross-validation is computationally

Algorithm 1: Bayesian functional graphical lasso Gibbs sampler

Input: Sum of the products matrix \mathbf{S} , i.e., $\mathbf{S} = \mathbf{Y}^T \mathbf{Y}$.
Output: MCMC sample of the precision matrix $\Theta^{(1)}, \dots, \Theta^{(L)}$.
Initialization: Set p to be number of nodes in graph, set initial values $\Theta^{(0)} = \mathbf{I}$, $\Sigma^{(0)} = \mathbf{I}$, $\mathbf{T}^{(0)} = \mathbf{J}$, where \mathbf{I} is $pM \times pM$ identity matrix and \mathbf{J} is a $pM \times pM$ matrix with all elements equal to one;
while *Convergence criteria are not met* **do**
 for $i = 1, \dots, p$ **do**
 Partition $\Theta^{(l)}$, \mathbf{S} and $\mathbf{T}^{(l)}$ into $p \times p$ blocks (focus on updating i th column block of Θ corresponding node i);
 for $j = 1, \dots, M$ **do**
 1. Partition $\Theta^{(l)}$, \mathbf{S} and $\mathbf{T}^{(l)}$ as in (15) and (17);
 2. Draw $\gamma^{(l+1)} \sim \text{Gamma}(\frac{n}{2} + 1, \frac{s_{22} + \lambda}{2})$;
 3. Draw $\beta^{(l+1)} \sim N_{(p-1)M}(-\mathbf{C}^{(l)} \bar{\mathbf{s}}_{21}, \mathbf{C}^{(l)})$, where
 $\mathbf{C}^{(l)} = ((\mathbf{D}_\tau^{(l)})^{-1} + (s_{22} + \lambda) \overline{\Theta_{11}^{-1}}^{(l)})^{-1}$;
 4. Update $\theta_{21}^{(l+1)} = (\beta^{(l+1)}, \mathbf{0})$, $\theta_{12}^{(l+1)} = (\theta_{21}^{(l+1)})^T$, $\theta_{22}^{(l+1)} = \gamma^{(l+1)} + (\beta^{(l+1)})^T \overline{\Theta_{11}^{-1}}^{(l+1)} \beta^{(l+1)}$;
 end
 Update $\mathbf{T}^{(l+1)}$ by sampling
 $(1/\tau_{ij}^2)^{(l+1)} | \Theta^{(l+1)}, \lambda \sim \text{Inverse Gaussian} \left(\sqrt{\frac{\lambda^2}{\|\Theta_{ij}^{(l+1)}\|_F^2}}, \lambda^2 \right)$ for $i, j = 1, \dots, p$
 end
 Store the realization of precision matrix $\Theta^{(l+1)}$;
 Increment $l \leftarrow l + 1$.
end

expensive, especially for Bayesian models implemented via MCMC. Further, Wasserman and Roeder (2009) show that cross-validation based on the log-likelihood loss function tends to lead to overfitting and unnecessarily dense graphs. Other than cross validation, approaches such as Akaike information criterion (AIC), Bayesian information criterion (BIC), and stability selection (Meinshausen et al., 2006) have been well studied in the graphical model literature. In the functional case, though, AIC/BIC does not work well, since it is unclear how to calculate the effective degrees of freedom. Thus, selecting an appropriate hyperparameter λ ahead of time is a nontrivial task. On the other hand, in the Bayesian framework, we can (for instance) assign a gamma prior $\lambda^2 \sim \text{Gamma}(s, r)$. In this case, the full conditional for λ is

$$\lambda^2 | \mathbf{T}, \Theta \sim \text{Gamma} \left(s + pM + \frac{p(p-1)(M^2+1)}{4}, r + \frac{\sum_l \theta_{ll} + \sum_{i < j} \tau_{ij}^2}{2} \right). \quad (22)$$

This can in turn be incorporated into the Gibbs sampler given in Algorithm 1 as an additional sampling step.

3.2 The Functional Graphical Horseshoe

In the presence of sparsity, as is often the case for precision matrices associated with GGMs, it is desirable to have a shrinkage approach that yields exact or values close to zero for the true null cases while simultaneously shrinking the truly non-zero cases as small as possible so that the resulting estimates have little bias. To address this desire, Carvalho et al. (2010) proposed the horseshoe prior. The prior has high probability concentration near zero and is heavy-tailed, properties that contribute to desired shrinkage behavior. Further, the prior can be expressed as a scale mixture of Gaussian distributions and thus is easily incorporated into a Gibbs sampler for posterior exploration. Carvalho et al. (2010) originally proposed the horseshoe for the sparse normal means model, but it was recently extended by Li et al. (2019) to estimation of GGMs. Li et al. (2019) established that the resulting horseshoe estimates are close to the unbiased least-square estimates with high probability and, further, that the Bayesian graphical lasso tends to be further away from the least squares estimates than the graphical horseshoe. In this section, we propose an extension of graphical horseshoe regularization to the case of functional graphical models.

We define the functional graphical horseshoe by using horseshoe priors on each off-diagonal block of the precision matrix and exponential priors on the diagonal elements. This yields the following prior:

$$\begin{aligned} \theta_{\ell,\ell} &\sim \text{Exp}(\lambda_{\ell,\ell}^2/2), \quad \ell = 1, \dots, pM \\ \boldsymbol{\theta}_{ij} &\stackrel{\text{indep.}}{\sim} N_{M^2}(\mathbf{0}, \lambda_{ij}^2 \tau^2 \mathbf{I}), \quad i, j = 1, \dots, p, \quad i \neq j \\ \lambda_{ij} &\stackrel{\text{iid}}{\sim} C^+(0, 1), \quad i, j = 1, \dots, p; \quad \tau \sim C^+(0, 1), \end{aligned} \tag{23}$$

where $\boldsymbol{\theta}_{ij} = \text{vec}(\boldsymbol{\Theta}_{ij})$ and $C^+(0, 1)$ represents the half-Cauchy distribution with density $p(x) \propto (1 + x^2)^{-1}$, $x > 0$. As in other versions of the horseshoe prior, the global shrinkage parameter τ is determined by the sparsity of the entire precision matrix, whereas the local shrinkage parameters λ_{ij} preserves blocks with $\|\boldsymbol{\Theta}_{ij}\| \neq 0$ by allowing them to be pulled toward zero considerably less than the zero blocks. Unlike Li et al. (2019), but similar to Wang (2012), we specify an $\text{Exp}(\lambda_{\ell,\ell}^2/2)$ prior for the diagonal elements of $\boldsymbol{\Theta}$. This is convenient for deriving the full conditional distributions and does not affect inference since the graph is determined by the off-diagonal elements.

The full conditional distribution of $\boldsymbol{\Theta}$ under the assumption of multivariate Gaussian likelihood is given by

$$\begin{aligned} p(\boldsymbol{\Theta} | \lambda, \Lambda, \tau, \mathbf{S}) &\propto |\boldsymbol{\Theta}|^{\frac{n}{2}} \exp \left\{ -\text{tr} \left(\frac{1}{2} \mathbf{S} \boldsymbol{\Theta} \right) \right\} \prod_{l=1}^p \frac{\lambda_{ll}^2}{2} \exp \left(-\frac{\lambda_{ll}^2}{2} \theta_{ll} \right) \\ &\times \prod_{i < j} N_{M^2}(\boldsymbol{\theta}_{ij} | \mathbf{0}, \lambda_{ij}^2 \tau^2 \mathbf{I}) C^+(\lambda_{ij} | 0, 1) \mathbf{1}_{\boldsymbol{\Theta} \in M^+}. \end{aligned} \tag{24}$$

where $\Lambda = \{\lambda_{ij}\}_{i,j=1}^p$. The standard technique for creating a straightforward Gibbs sampler with the horseshoe is to use the realization of Makalic and Schmidt (2016) that if $x^2 | a \sim \text{inverse Gamma}(1/2, 1/a)$ and $a \sim \text{inverse Gamma}(1/2, 1/A^2)$, then, marginally, $x \sim C^+(0, A)$. Thus, we introduce latent variables ν_{ij} and ζ to facilitate conditional conjugacy when updating the shrinkage parameters λ_{ij} and τ .

Under the parameter-expanded hierarchical model, the full conditional distribution of the precision matrix is given by

$$\begin{aligned}
p(\Theta | \mathbf{S}, \mathbf{\Lambda}, \tau, \boldsymbol{\nu}, \zeta) &\propto |\Theta|^{\frac{n}{2}} \exp \left\{ -\text{tr} \left(\frac{1}{2} \mathbf{S} \Theta \right) \right\} \prod_{l=1}^p \frac{\lambda_{l,l}^2}{2} \exp \left(-\frac{\lambda_{l,l}^2}{2} \theta_{ll} \right) \\
&\times \prod_{i < j} N_{M^2}(\boldsymbol{\theta}_{ij} | \mathbf{0}, \lambda_{ij}^2 \tau^2 \mathbf{I}) \prod_{i < j} \nu_{ij}^{-\frac{1}{2}} \lambda_{ij}^{-3} \exp \left(-\frac{1}{\lambda_{ij}^2 \nu_{ij}} \right) \nu_{ij}^{-\frac{3}{2}} \exp \left(-\frac{1}{\nu_{ij}} \right) \\
&\times \zeta^{-\frac{1}{2}} \tau^{-3} \exp \left(-\frac{1}{\tau^2 \zeta} \right) \zeta^{-\frac{3}{2}} \exp \left(-\frac{1}{\zeta} \right).
\end{aligned} \tag{25}$$

We can use a data-augmented Gibbs sampler with the same matrix permutation as used for the Bayesian fglasso proposed in Subsection 3.1.

In each iteration, the rows and columns of the Mp -dimensional matrices Θ , \mathbf{S} , $\mathbf{\Lambda} = \{\lambda_{ij}^2\}_{p \times p} \otimes \mathbf{J}_{M \times M}$, and $\mathbf{V} = \{\nu_{ij}^2\}_{p \times p} \otimes \mathbf{J}_{M \times M}$ are partitioned the same way as in Subsection 3.1 to derive the full conditional distributions; i.e.,

$$\begin{aligned}
\Theta &= \begin{bmatrix} \Theta_{11} & \boldsymbol{\theta}_{12} \\ \boldsymbol{\theta}_{12}^T & \theta_{22} \end{bmatrix}, \quad \mathbf{S} = \begin{bmatrix} \mathbf{S}_{11} & \mathbf{s}_{12} \\ \mathbf{s}_{12}^T & s_{22} \end{bmatrix}, \\
\mathbf{\Lambda} &= \begin{bmatrix} \mathbf{\Lambda}_{11} & \boldsymbol{\lambda}_{12} \\ \boldsymbol{\lambda}_{12}^T & \lambda_{22} \end{bmatrix}, \quad \mathbf{V} = \begin{bmatrix} \mathbf{V}_{11} & \boldsymbol{\nu}_{12} \\ \boldsymbol{\nu}_{12}^T & \nu_{22} \end{bmatrix},
\end{aligned} \tag{26}$$

where the blocks are arranged as before. The derivation of full conditionals for the last column $\boldsymbol{\theta}_{12}$ and θ_{22} is similar to the Bayesian fglasso by changing variables. The conditional distribution of nonzero variables of the last column in Θ is

$$p(\bar{\boldsymbol{\theta}}_{12}, \theta_{22} | -) \propto \left(\theta_{22} - \bar{\boldsymbol{\theta}}_{12}^T \bar{\boldsymbol{\Theta}}_{11}^{-1} \bar{\boldsymbol{\theta}}_{12} \right)^{\frac{n}{2}} \exp \left\{ -\frac{1}{2} [\bar{\boldsymbol{\theta}}_{12}^T \mathbf{D}_\tau^{-1} \bar{\boldsymbol{\theta}}_{12} + 2 \bar{\mathbf{s}}_{12}^T \bar{\boldsymbol{\theta}}_{12} + (s_{22} + \lambda_{22}^2) \theta_{22}] \right\}, \tag{27}$$

where $\mathbf{D}_\tau = \tau^2 \text{diag}(\bar{\boldsymbol{\lambda}}_{12})$. Making a change of variables by $\boldsymbol{\beta} = \bar{\boldsymbol{\theta}}_{12}$, $\gamma = (\theta_{22} - \bar{\boldsymbol{\theta}}_{12}^T \bar{\boldsymbol{\Theta}}_{11}^{-1} \bar{\boldsymbol{\theta}}_{12})$, and letting $\mathbf{C} = (\mathbf{D}_\tau^{-1} + (s_{22} + \lambda_{22}^2) \bar{\boldsymbol{\Theta}}_{11}^{-1})^{-1}$, then the full conditional of $\boldsymbol{\beta}, \gamma$ is

$$\boldsymbol{\beta}, \gamma | - \sim N_{(p-1)M}(-\mathbf{C} \bar{\mathbf{s}}_{21}, \mathbf{C}) \text{Gamma} \left(\frac{n}{2} + 1, \frac{s_{22} + \lambda_{22}^2}{2} \right) \tag{28}$$

As for the Bayesian fglasso, we first cycle through all columns corresponding to the same node, then move to next node. After the entire Θ is updated, the local and global shrinkage parameters λ_{ij} and τ need to be sampled. Through conditional conjugacy, the full conditional distributions of $\lambda_{ij}, \nu_{ij}, \tau^2$, and ζ are quickly seen to be inverse Gamma. The condition $\Theta \in M^+$ is maintained during each iteration as long as the starting value is positive definite, for the same reason that positive definite constraint is satisfied in the Bayesian fglasso sampler. The full Gibbs sampler is summarized in Algorithm 2.

4 Numerical Experiments

We designed simulation studies to assess the performance of posterior inference using the Bayesian functional graphical lasso and horseshoe outlined in Section 3. For our simulation studies, we considered different sample sizes ($N = 5, 20, 100, 200$), graph sizes ($p =$

10, 30, 50), two different types of networks, and both sparse- and dense-sampled functions. This allows us to compare the frequentist fglasso of Qiao et al. (2019), Bayesian fglasso, and functional graphical horseshoe to each other across a variety of scenarios. We assess classification accuracy and fidelity of the estimates of both the zero and non-zero entries of the precision matrices in Subsection 4.1. As a matter of practicality for researchers interested in implementing the proposed techniques, we also compare the computational expense associated with each procedure across different computing environments (R, NumPy, and TensorFlow) in Subsection 4.2.

4.1 Estimation and Classification

Similar to the simulation studies considered by Qiao et al. (2019), we simulate functional data with $g_{ij}(t) = \mathbf{s}(t)^T \boldsymbol{\delta}_{ij}$, $i = 1, \dots, n$, $j = 1, \dots, p$, where $\mathbf{s}(t) \in \mathbb{R}^5$ contains the first five Fourier basis functions, and $\boldsymbol{\delta}_{ij} \in \mathbb{R}^5$ is a zero mean Gaussian random vector. Hence, $\boldsymbol{\delta}_i = (\boldsymbol{\delta}_{i1}^T, \dots, \boldsymbol{\delta}_{ip}^T)^T \in \mathbb{R}^{5p}$ follows a multivariate Gaussian distribution with covariance matrix $\boldsymbol{\Sigma} = \boldsymbol{\Theta}^{-1}$, where the underlying graph is determined by the sparsity pattern of $\boldsymbol{\Theta}$. We consider here two types of networks:

- *Network 1:* A block banded matrix $\boldsymbol{\Theta}$ with $\boldsymbol{\Theta}_{jj} = \mathbf{I}_5$, $\boldsymbol{\Theta}_{j,j-1} = \boldsymbol{\Theta}_{j-1,j} = 0.4\mathbf{I}_5$, and $\boldsymbol{\Theta}_{j,j-2} = \boldsymbol{\Theta}_{j-2,j} = 0.2\mathbf{I}_5$ for $j = 1, \dots, p$, and 0 elsewhere. The network results in each node being connected to its immediate neighbors, and weaker connection to its second-order neighbors.
- *Network 2:* For $j = 1, \dots, 10, 21, \dots, 30, \dots$, the corresponding submatrices in $\boldsymbol{\Theta}$ are the same as those in Network 1 with $p = 10$, indicating every alternating block of 10 nodes are connected as Network 1. For $j = 11, \dots, 20, 31, \dots, 40, \dots$, we set $\boldsymbol{\Theta}_{jj} = \mathbf{I}_5$, so the remaining nodes are fully isolated.

For each network, we generate n realizations of $\boldsymbol{\delta} \sim N_{5p}(\mathbf{0}, \boldsymbol{\Theta}^{-1})$. The observed data are then generated as $h_{ijk} = g_{ij}(t_{ik}) + e_{ijk}$, $e_{ijk} \sim N(0, 0.5^2)$, $k = 1, \dots, T$, where subject i was observed at time points $t_{i1}, \dots, t_{iT} \in [0, 1]$. We consider two sampling schemes from the functions:

- *Dense design with equally spaced measurements:* Each function was recorded on a regular grid between 0 and 1, i.e., $t_{i1} = 0, \dots, t_{iT} = 1$ and $T = 100$, $i = 1, \dots, N$.
- *Sparse design with irregularly-spaced measurements:* Each function was recorded randomly; i.e., t_{ik} are drawn randomly between 0 and 1 for $k = 1, \dots, 9$.

Our proposed graphical models work with any choice of basis representation, but we choose the data-driven functional PCA approach, due to the mean-square optimality discussed in Section 2.2 and the smoothness of the simulated data. Thus, to implement any of the approaches considered, we need to compute the first M estimated principal components scores of g_{ij} . We use the PACE algorithm (Yao et al., 2005) for the irregularly sampled setting via the `fdapace` package in R (Carroll et al., 2020). For the regularly sampled case,

we use ordinary singular value decomposition. We determine the truncation level M in (7) using the minimum number of principal component to capture 95% of the variability over all nodes for the SVD method and PACE algorithm. For both the Bayesian functional graphical lasso and the Bayesian functional graphical horseshoe, a total of 10,000 MCMC iterations are performed after 1000 burn-in iterations. Convergence is assessed via trace plots of randomly selected elements of Θ .

We first compare the frequentist fglasso to our proposed Bayesian fglasso model with a fixed regularization parameter λ . The primary differences then are the point estimates of Θ (MAP estimate versus posterior mean) and the thresholding rule used to select the graph. With MAP estimation, the zeros are automatically produced as part of the optimization. For the Bayesian procedure, elementwise equal-tailed credible intervals are constructed from the MCMC output, whence elements of Θ are selected via those intervals that do not contain zero. For both methods and for a grid of λ values, we compute the true positive rate, $TPR_\lambda = TP/(TP + FN)$, and false positive rate, $FPR_\lambda = FP/(FP + TN)$, where TP and TN stand for true positives and negatives, respectively in terms of network edges correctly identified, and similarly for FP and FN . With these measures we can compute the areas under the associated ROC curves (AUCs), where values closer to 1 indicate better discriminative power between the true zero and non-zero edges in the true graph.

Table 1 displays the AUC values for the various settings described above. As expected from the correspondence between the frequentist and Bayesian formulations of the objective, we see very similar performance between the two approaches across each scenario considered. This suggests that, as far as graphical model selection is concerned, the frequentist and Bayesian implementations of the fglasso have equivalent discriminative ability with fixed a regularization parameter. However, the Bayesian approach facilitates additional flexibility in how the regularization parameter is treated. While it is possible to estimate λ with, e.g., cross-validation, it can be computationally expensive to do so. On the other hand, assigning a prior distribution to the regularization term, or circumventing an explicit λ altogether via, e.g., the horseshoe, allows the appropriate penalty to be learned from the data along with the remaining parameters in the model, so that it only needs to be fit once. We consider this approach next.

Having compared the frequentist and Bayesian versions of the fglasso with a fixed regularization parameter, we turn our attention to a direct comparison between the Bayesian fglasso and the functional graphical horseshoe. One advantage of the horseshoe prior is that the global/local shrinkage in the model automatically adapts to the observed data. To allow for such “automatic” adaptation in the Bayesian fglasso, we use the augmented version of the model in which a hyperprior is assigned, $\lambda^2 \sim \text{Gamma}(1, 0.01)$. In this comparison, we consider fpc scores generated from $p = 10$ nodes with $N = 100$ observations and rank $M = 5$ in the basis expansion, using Network 1 defined above. We recognize that selection via credible intervals under the horseshoe tends to be conservative and that the width of the intervals tends to grow with size of the true signal (Van Der Pas et al., 2014). Thus, following Li et al. (2019) for each model, 50% equal-tailed credible intervals were constructed and used as the basis for graph selection.

Figure 1 depicts the interval estimates for the off-diagonal elements, separated by the true zeros, those with weight 0.2, and those with weight 0.4. We can make several observations from this figure. First, the thresholding rule with the Bayesian fglasso results in an extremely

large number of false positives, compared to the much lower false positive rate with the same rule applied to the functional graphical horseshoe. Thus, the Bayesian functional graphical lasso exhibits behavior similar to that which is known about its scalar counterpart. The stronger mass near the origin applied by the horseshoe compared to the Bayesian graphical lasso (Li et al., 2019, Theorem 3.2) results in much better identification of the true zeros in the model. Second, for the truly non-zero entries in Θ , all of the functional graphical horseshoe credible intervals fail to capture the true weight, whereas many of the corresponding intervals under the Bayesian fglasso do capture the true non-zero values. This does not necessarily suggest superior estimation fidelity, however. Indeed, the fact that the Bayesian fglasso intervals capture more of the non-zero weights is mostly due to the much lower precision (wider intervals) associated with the estimators, as opposed to the generally much narrower intervals around the functional graphical horseshoe estimates. In this case, we see the width of the functional graphical horseshoe credible intervals growing as the signal size goes from 0.2 to 0.4, as would be expected from the results of Van Der Pas et al. (2014), whereas the hierarchical Bayesian fglasso exhibits no such behavior. Performance characteristics are quantified in Table 2. In terms of mean squared error of the estimates, the horseshoe again shows very faithful recovery of the true zeros due to its local-global shrinkage property. For the non-zero estimates, however, we observe smaller estimation error with the Bayesian fglasso than with the functional graphical horseshoe, though both are small relative to the signal strength. The Bayesian fglasso has 1% and 8% relative errors for the 0.2 and 0.4 weights, respectively, whereas the functional graphical horseshoe has 16% and 13% relative errors, respectively.

Figure 1 and Table 2 suggest that the Bayesian fglasso may be preferable for estimating the truly non-zero elements. In practice, though, one will not know which elements are truly non-zero. The true non-zero cases found by the Bayesian fglasso may be lost in the large number of false positives. On the other hand, the functional graphical horseshoe does a much better job of avoiding false positives, at the expense of stronger estimation error of the true non-zero cases due to the stronger shrinkage toward zero. We remark that this behavior is not contradictory to previously established results concerning the Bayesian lasso, graphical lasso, horseshoe, or graphical horseshoe. Indeed, the theoretical work on the Bayesian (graphical) lasso of which we are aware considers a fixed regularization parameter λ , whereas the Bayesian fglasso considered here used a $\text{Gamma}(1, 0.01)$ prior on the regularization parameter. The performance with a hyper-prior on the regularization term is not at all well understood, and it is likely that different prior specification could yield different results. The functional graphical horseshoe does not suffer from such subjective specification, though, since the horseshoe prior effectively circumvents the specification issue altogether through the more objective half-Cauchy priors on the global and local shrinkage parameters. We also emphasize that, while the Bayesian graphical lasso and graphical horseshoe have received previous attention in the literature, here we are considering graphical models associated with functional data. Such cases are less understood from either a frequentist or a Bayesian perspective.

Next we compare the frequentist fglasso to the hierarchical Bayesian fglasso (as opposed to the fixed- λ Bayesian fglasso considered above) and the functional graphical horseshoe in terms of misclassification error and graph similarity when the regularization parameter is determined as it would be in practice. The frequentist fglasso requires tuning of the regular-

ization parameter, either through cross-validation or by setting it to yield a desired sparsity level. For the frequentist fglasso we use 10-fold cross-validation for model selection, since in practice the *true* sparsity of the underlying graph will most likely be unknown. As the Bayesian fglasso behaves differently than the horseshoe, and to reduce the number of false positives, we use 90% credible intervals for the hierarchical Bayesian fglasso. As before, we use 50% credible intervals for thresholding with the functional graphical horseshoe. Table 3 reports the false positive rate (FPR), false negative rate (FNR), overall misclassification rate, the F1 score (also known as Dice coefficient), and resulting sparsity levels for $p = 10, 30, 50$ nodes, and $N = 100$ subjects with densely-sampled functions under both Network 1 and 2. The scores are averaged over 10 replications of each scenario. With the exception of $p = 10$ nodes in Network 2, the functional graphical horseshoe always has the highest F1 score, indicating the strongest graph similarity. We further see that the functional graphical horseshoe has the results with closest sparsity level to the true sparsity level. The frequentist fglasso generally performs the worst, due to the overly dense graphs that it produces, reflecting known risks of using log-likelihood-based cross-validation in this type of model (Wasserman and Roeder, 2009).

4.2 Computational Cost

Lastly, as a pragmatic matter, we evaluate the computational speed and the scalability of our proposed block Gibbs samplers in three different environments, **R**, **NumPy**, and **TensorFlow**. Our proposed Gibbs sampler for the functional graphical horseshoe has similar computational complexity as the Bayesian fglasso, so we only show the results of Bayesian functional graphical lasso. We use simulated data from Network 1 with $N = 100$ and rank $M = 5$ while varying the number of nodes up to $p = 300$. All computations are run on a standard x86 machine (28-core CPU with 120G memory), using **R** or **Python**. For each such simulated data set, we measure the wall time required to generate 2,000 full iterations of the Gibbs sampler. We provide implementation code for the different environments at <https://github.com/jjniu/BayesFGM>.

Figure 2 displays the results, where the right panel is on the log scale for $p = 1, \dots, 100$ for finer distinction. It takes about 1.9 min, 0.72 min, and 9 min to generate 2,000 iterations under $p = 10$ nodes with **R**, **NumPy** and **TensorFlow**, respectively. On the other hand, with $p = 200$, pure **R** takes 262.29 hours, **NumPy** takes 128.12 hours, and **TensorFlow** takes 53.5 hours. In general, we see that **TensorFlow** is the slowest language with small graphs, but that it also scales at a much lower rate than **NumPy** or **R**. Of the approaches considered, **NumPy** is the fastest for graphs of size up to $p \approx 100$, but **TensorFlow** is preferable for extremely large graphs. It is no surprise that base **R** is the slowest and scales at the worst rate. **R** is known for its tendency to be slow with iteration-intense tasks due to its repeated data type conversion on each iteration. It is likely that interfacing **R** with **C++** via the **Rcpp** package (Eddelbuettel and François, 2011) would yield much better results when working in pure **R**, but we did not consider that approach here.

5 Applications

5.1 Alcoholism Study

Here we apply our proposed functional graphical horseshoe method to an event-related potential electroencephalography (EEG) dataset from an alcoholism study originally reported by Zhang et al. (1995). The data, freely available at <https://archive.ics.uci.edu/ml/datasets/eeg+database>, consist of 122 subjects, 77 of whom were identified as alcoholics, and 45 in the control group. Signals were initially collected from 64 electrodes placed on subjects’ scalps at standard positions, and captured voltage signals at 256 Hz during a one-second time period. 120 trials were collected per subject. During each trial, the subject was exposed to either a single stimulus (a single picture) or two stimuli (a pair of pictures) shown on a computer monitor. The interest here is in estimating a graphical network representing functional connections between different brain regions. Assuming that the data $g_1(t), \dots, g_{64}(t)$ jointly follow from a 64-dimensional multivariate Gaussian process (MGP), Zhu et al. (2016) and Qiao et al. (2019) both analyzed the data via functional graphical model methodology. We filtered the signals through a banded filter between to obtain α frequencies between 8 and 12.5 Hz, as the α band has been shown to differentiate between alcoholic and control groups under this task. Moreover, we take the average of all trials for each subject, resulting in a single event-related potential curve at each electrode for each subject. The filtering was performed by applying the `eegfilter` function in the `eegkit` package (Helwig, 2018) in R. Since the data are regularly and densely sampled, we employed the regular SVD method to compute the principal component scores $\hat{\mathbf{a}}$. The truncated number of fpcs are selected so that at least 95% of the variation in the filtered signal trajectories for control and alcoholic curves are captured by the basis representations. For each MCMC run, 10,000 iterations were retained after an initial burn-in period of 1000 iterations. To be conservative and achieve a higher level of sparsity, the edges are selected via 90% credible intervals.

The results are summarized in Figure 3. The weight of each edge is evaluated as the Frobenius norm of the estimated precision matrix for that edge; i.e., $(\|\hat{\Theta}_{ij}\|_F)_{p \times p}$. In the weighted graphs, thicker edges indicate larger weights. Among the selected edges, 153 edges are identified by both alcoholic and control graphs, denoted by orange lines in both graphs. We can see that most of the common edges have strong weights. By contrasting the alcoholic and control graphs, we see that the alcoholic group contains more edges connecting the frontal-central regions than the control group. It also appears that the right parietal region tends to have more connection in the alcoholic group than in the control group. Finding a more densely connected frontal region and differences in the right parietal region agrees with that which was found by Zhu et al. (2016). There are clear differences, of course, just as there were between functional graphical models estimated by Qiao et al. (2019) and Zhu et al. (2016). We remark that Qiao et al. (2019) specifically tuned their functional graphical lasso to obtain only 5% sparsity for ease of presentation. Overall, however, we find qualitative agreement with the analysis of Zhu et al. (2016), despite the fact that their assumed model was quite different from our functional graphical horseshoe, and the fact that our approach does not assume a decomposable graph.

5.2 Structural Connectivity after Traumatic Brain Injury

It is known that traumatic brain injuries can cause acute disconnections in white matter tracts (Rutgers et al., 2008), and there is interest in studying what happens to these connections during the chronic phase after such injuries. To address this question, we applied our proposed Bayesian functional graphical horseshoe to diffusion tensor imaging data (DTI) obtained from the Alzheimer’s Disease Neuroimaging Initiative (ADNI). The data consist of 34 subjects, 17 of whom have been identified as having experienced traumatic brain injury (TBI) with the remaining 17 being healthy controls. The control subjects were selected from a much larger group via propensity score matching to control for confounding variables such as patient’s age, sex, whole brain volume, and Alzheimer’s disease status. The data contain initial and follow-up measurements of fractional anisotropy in each of $p = 26$ regions of interest (ROI) in the brain, resulting in irregularly measured longitudinal data for each ROI. For each subject, anywhere from one to nine time points are available, each separated by several months. The data preprocessing includes eddy-correction (Andersson and Sotiropoulos, 2016), brain extraction, (Smith, 2002) and intensity normalization (Jenkinson and Smith, 2001; Jenkinson et al., 2002). For each voxel in a brain image, the fractional anisotropy (FA) is calculated as $FA = (3/2)((\lambda_1 - \bar{\lambda})^2 + (\lambda_2 - \bar{\lambda})^2 + (\lambda_3 - \bar{\lambda})^2)^{1/2}(\lambda_1^2 + \lambda_2^2 + \lambda_3^2)^{-1/2}$, where λ_1, λ_2 and λ_3 are the eigenvalues associated with the $x-$, $y-$ and $z-$ directions of the diffusion tensor and $\bar{\lambda} = \frac{\lambda_1 + \lambda_2 + \lambda_3}{3}$ is the mean diffusivity. FA indicates the degree of anisotropy of a diffusion process valued between 0 and 1. If the FA is close to 0, the diffusion is unrestricted in all directions, indicating loosely structured (i.e., deteriorated) white matter, whereas FA close to 1 means that the diffusion mainly occurs only along one axis, thus indicating stronger white matter in that area. The voxel-wise FA values are averaged to summarize the observed FA in each ROI at each time point. In total, we focus on exploring the connectivity (conditional dependence in brain atrophy) between 52 ROIs. Each ROI considered is listed in Table 4.

Similar to the EEG study, we assume the longitudinal data $g_1(t), \dots, g_{52}(t)$ jointly follow a 52-dimensional MGP. We use the PACE algorithm to carry out FPCA, where the truncation level of fpc scores is selected by capturing 95% of the variance in the curves. Then we fit our functional graphical horseshoe model via the Gibbs sampler discussed in 3.2, running the MCMC for 100,000 iterations after an initial 10,000-iteration burn-in period. The estimated graphs are constructed based on 50% credible intervals from the approximate posterior sample.

The estimated FA networks for the TBI and control groups are plotted in Figure 4. The sparsity levels for the TBI and control groups are 15.99% (212 edges) and 8.45% (112 edges), respectively. Forty edges are common to both graphs, indicated by orange lines in the figure. The TBI group tends to have more connections between different ROIs, particularly within right hemisphere. In most types of brain damage and dysfunction, performance IQ (PIQ) tends to deteriorate faster than verbal IQ (VIQ), leading to a PIQ/VIQ discrepancy. The increased connectivity in the right hemisphere observed here may reflect degraded right hemisphere functioning as PIQ deteriorates.

We see overall a denser set of connections in the TBI group than in the healthy controls. This agrees with results reported by Kook et al. (2021) in a study of children with a history of TBI compared to a group with extra-cranial injury. The increased structural connectivity

observed here in the TBI patients may reflect so-called “axonal sprouting” occurring as disconnected neurons attempt to reconnect to a network from which they have been isolated. This results in “improved” connectivity, but nevertheless a deterioration of functional activation and task performance. It is also possible that there are no entirely new structural connections between areas, but that the weight of the white matter tracts in the areas may increase, on average, because targeted selection of cortical modules necessary to participate in a given task breaks down in the presence of a brain injury. Indeed, enlargement of the activation field in stroke recovery has been observed in the literature (Lindow et al., 2016). Our results here support the previously observed phenomenon in which white matter tracts evince increased connectivity in the chronic phase after disconnection of the tracts in the acute phase (Rutgers et al., 2008).

6 Conclusion

In this article, we consider a Bayesian framework for graphical models associated with functional data. We proposed a fully Bayesian version of the functional graphical lasso as well as a novel functional graphical horseshoe prior. We provide also easily implemented Gibbs samplers via auxiliary variables to induce conditional conjugacy and adapting matrix partitioning techniques that have been used for other MCMC implementations of Bayesian graphical models. We compared these models to each other in several simulated scenarios. The Bayesian fglasso with fixed regularization term and the frequentist fglasso performed almost identically in terms of edge selection, as would be expected, with the exception that the Bayesian approach allows access to the full posterior distribution so that any quantity of interest can be obtained, not just the posterior mode. The hierarchical Bayesian extension of the fglasso and the functional graphical horseshoe were directly compared to each other. The simulation results demonstrated that the functional graphical horseshoe is much better at avoiding false positives than either the frequentist or Bayesian fglasso and is still able to detect relatively weak signals. The superior balance between false positives and false negatives results in the functional graphical horseshoe exhibiting generally superior similarity to the underlying true graph. We also applied the functional graphical horseshoe to two applications in neuroimaging, one a previously studied EEG example, and the other involving DTI measurements to compare white matter integrity in people with and without a history of traumatic brain injury.

The ability of the functional graphical horseshoe to avoid false positives is a critical characteristic for application in functional neuroimaging, as this field is often criticized for its abundance of false positives (Eklund et al., 2016). In addition, both EEG and MRI are notorious for having weak signal-to-noise ratios, making methods that are powerful at detecting weak signals quite useful. Indeed, the results in Section 5.2 suggest that our proposed methods may be helpful for understanding functional reorganization, a process in which many weak connections form.

While our work here suggests promising results, especially with extending the graphical horseshoe to functional graphical models, much work still remains. Our proposed Gibbs samplers are efficient in small to moderately-sized scenarios, but the computational experiments show the practical limits as the size of the graph grows large, regardless of the programming

environment used. One future line of research would be to explore more computationally efficient MCMC techniques for exploring the posterior distributions, or other posterior approximation methods appropriate for extremely high dimensional problems. There also remains deeper theoretical development of Bayesian approaches to functional graphical models, which to date is very limited.

Acknowledgment

Data collection and sharing for this project was funded by the Alzheimer’s Disease Neuroimaging Initiative (ADNI) (National Institutes of Health Grant U01 AG024904) and DOD ADNI (Department of Defense award number W81XWH-12-2-0012). ADNI is funded by the National Institute on Aging, the National Institute of Biomedical Imaging and Bioengineering, and generous private sector contributions. DAB is partially supported by the National Science Foundation (NSF) Grant OIA-1826715. The content is solely the responsibility of the authors and does not necessarily represent the official views of the funding agencies.

References

- Andersson, J. L. and S. N. Sotiropoulos (2016). An integrated approach to correction for off-resonance effects and subject movement in diffusion mr imaging. *Neuroimage* 125, 1063–1078.
- Banerjee, O., L. El Ghaoui, and A. d’Aspremont (2008). Model selection through sparse maximum likelihood estimation for multivariate gaussian or binary data. *Journal of Machine Learning Research* 9, 485–516.
- Banerjee, S. and S. Ghosal (2014). Posterior convergence rates for estimating large precision matrices using graphical models. *Electronic Journal of Statistics* 8(2), 2111–2137.
- Bosq, D. (2012). *Linear processes in function spaces: theory and applications*, Volume 149. Springer Science & Business Media.
- Carroll, C., A. Gajardo, Y. Chen, X. Dai, J. Fan, P. Z. Hadjipantelis, K. Han, H. Ji, H.-G. Mueller, and J.-L. Wang (2020). *fdapace: Functional Data Analysis and Empirical Dynamics*. R package version 0.5.5.
- Carvalho, C. M., N. G. Polson, and J. G. Scott (2010). The horseshoe estimator for sparse signals. *Biometrika* 97(2), 465–480.
- Dawid, A. P. and S. L. Lauritzen (1993). Hyper markov laws in the statistical analysis of decomposable graphical models. *Annals of Statistics* 21(3), 1272–1317.
- Dempster, A. P. (1972). Covariance selection. *Biometrika* 32, 95–108.
- Eddelbuettel, D. and R. François (2011). Rcpp: Seamless R and C++ integration. *Journal of Statistical Software* 40(8), 1–18.

- Eklund, A., T. E. Nichols, and H. Knutsson (2016). Cluster failure: Why fMRI inferences for spatial extent have inflated false-positive rates. *Proceedings of the National Academy of Sciences* 113(28), 7900–7905.
- Friedman, J., T. Hastie, and R. Tibshirani (2008). Sparse inverse covariance estimation with the graphical lasso. *Biostatistics* 9(3), 432–441.
- Gelfand, A. E. and A. F. Smith (1990). Sampling-based approaches to calculating marginal densities. *Journal of the American Statistical Association* 85(410), 398–409.
- Greenlaw, K., E. Szefer, J. Graham, M. Lesperance, F. S. Nathoo, and A. D. N. Initiative (2017). A bayesian group sparse multi-task regression model for imaging genetics. *Bioinformatics* 33(16), 2513–2522.
- Helwig, N. (2018). eegkit: Toolkit for electroencephalography data. URL: <http://CRAN.R-project.org/package=eegkit>. R package version, 1–0.
- Jenkinson, M., P. Bannister, M. Brady, and S. Smith (2002). Improved optimization for the robust and accurate linear registration and motion correction of brain images. *Neuroimage* 17(2), 825–841.
- Jenkinson, M. and S. Smith (2001). A global optimisation method for robust affine registration of brain images. *Medical image analysis* 5(2), 143–156.
- Jolliffe, I. (2002). *Principal Component Analysis* (2nd ed.). New York: Springer.
- Karhunen, K. (1946). Zur Spektraltheorie Stochastischer Prozesse. *Annales Academiae Scientiarum Fennicae* 34, 1–7.
- Knight, K. and W. Fu (2000). Asymptotics for lasso-type estimators. *Annals of statistics*, 1356–1378.
- Kook, J. H., K. A. Vaughn, D. M. DeMaster, L. Ewing-Cobbs, and M. Vannucci (2021). Bvar-connect: A variational bayes approach to multi-subject vector autoregressive models for inference on brain connectivity networks. *Neuroinformatics* 19, 39–56.
- Kyung, M., J. Gill, M. Ghosh, G. Casella, et al. (2010). Penalized regression, standard errors, and bayesian lassos. *Bayesian Analysis* 5(2), 369–411.
- Lam, C. and J. Fan (2009). Sparsistency and rates of convergence in large covariance matrix estimation. *Annals of statistics* 37(6B), 4254.
- Li, Y., B. A. Craig, and A. Bhadra (2019). The graphical horseshoe estimator for inverse covariance matrices. *Journal of Computational and Graphical Statistics*, 1–24.
- Lindow, J., M. Domin, M. Grothe, U. Horn, S. B. Eickhoff, and M. Lotze (2016). Connectivity-based predictions of hand motor outcome for patients at the subacute stage after stroke. *Frontiers in human neuroscience* 10, 101.
- Loeve, M. (1963). *Probability Theory*. Van Nostrand.

- Makalic, E. and D. F. Schmidt (2016). A simple sampler for the horseshoe estimator. *IEEE Signal Processing Letters* 23, 179–182.
- Meinshausen, N., P. Bühlmann, et al. (2006). High-dimensional graphs and variable selection with the lasso. *The annals of statistics* 34(3), 1436–1462.
- Qiao, X., S. Guo, and G. M. James (2019). Functional graphical models. *Journal of the American Statistical Association* 114(525), 211–222.
- Rajaratnam, B., H. Massam, and C. M. Carvalho (2008). Flexible covariance estimation in graphical gaussian models. *The Annals of Statistics* 36(6), 2818–2849.
- Rue, H. and L. Held (2005). *Gaussian Markov random fields: theory and applications*. CRC press.
- Rutgers, D., F. Toulgoat, J. Cazejust, P. Fillard, P. Lasjaunias, and D. Ducreux (2008). White matter abnormalities in mild traumatic brain injury: a diffusion tensor imaging study. *American Journal of Neuroradiology* 29(3), 514–519.
- Shappell, H., B. S. Caffo, J. J. Pekar, and M. A. Lindquist (2019). Improved state change estimation in dynamic functional connectivity using hidden semi-markov models. *NeuroImage* 191, 243–257.
- Smith, S. M. (2002). Fast robust automated brain extraction. *Human brain mapping* 17(3), 143–155.
- Tibshirani, R. (1996). Regression shrinkage and selection via the lasso. *Journal of the Royal Statistical Society: Series B (Methodological)* 58(1), 267–288.
- Van Der Pas, S. L., B. J. Kleijn, and A. W. Van Der Vaart (2014). The horseshoe estimator: Posterior concentration around nearly black vectors. *Electronic Journal of Statistics* 8(2), 2585–2618.
- Vandenberghe, L., S. Boyd, and S.-P. Wu (1998). Determinant maximization with linear matrix inequality constraints. *SIAM journal on matrix analysis and applications* 19(2), 499–533.
- Wang, H. (2012). Bayesian graphical lasso models and efficient posterior computation. *Bayesian Analysis* 7(4), 867–886.
- Wasserman, L. and K. Roeder (2009). High dimensional variable selection. *Annals of statistics* 37(5A), 2178.
- Xiang, R., K. Khare, and M. Ghosh (2015). High dimensional posterior convergence rates for decomposable graphical models. *Electronic Journal of Statistics* 9(2), 2828–2854.
- Yao, F., H.-G. Müller, and J.-L. Wang (2005). Functional data analysis for sparse longitudinal data. *Journal of the American Statistical Association* 100(470), 577–590.

- Yuan, M. and Y. Lin (2006). Model selection and estimation in regression with grouped variables. *Journal of the Royal Statistical Society: Series B (Statistical Methodology)* 68(1), 49–67.
- Yuan, M. and Y. Lin (2007). Model selection and estimation in the Gaussian graphical model. *Biometrika* 94(1), 19–35.
- Zhang, L., V. Baladandayuthapani, Q. Neville, K. Quevedo, and J. S. Morris (2021). Bayesian functional graphical models. arXiv preprint arXiv:2108.05034.
- Zhang, X. L., H. Begleiter, B. Porjesz, W. Wang, and A. Litke (1995). Event related potentials during object recognition tasks. *Brain Research Bulletin* 38(6), 531–538.
- Zhu, H., N. Strawn, and D. B. Dunson (2016). Bayesian graphical models for multivariate functional data. *The Journal of Machine Learning Research* 17(1), 7157–7183.
- Zhu, Y., X. Shen, and W. Pan (2014). Structural pursuit over multiple undirected graphs. *Journal of the American Statistical Association* 109(508), 1683–1696.

Algorithm 2: Bayesian functional graphical horseshoe Gibbs sampler

Input: Sum of the products matrix \mathbf{S} , i.e., $\mathbf{S} = \mathbf{Y}^T \mathbf{Y}$.

Output: Samples of precision matrix $\hat{\Theta}$.

Initialization: Set p to be number of nodes in graph, set initial values $\Theta = \mathbf{I}$, $\Sigma = \mathbf{I}$, $\Lambda = \mathbf{J}$, $\mathbf{V} = \mathbf{J}$, where \mathbf{I} is $pM \times pM$ identity matrix and \mathbf{J} is a $pM \times pM$ matrix with all elements equal to one;

while Given the current $\Theta \in M^+$ and τ , repeat for a large number of iterations until convergence is achieved **do**

for $i = 1, \dots, p$ **do**

 Partition Θ , \mathbf{S} , \mathbf{T} and \mathbf{V} into $p \times p$ blocks (focus on updating i th column block of Θ corresponding node i and all the other nodes);

 1. **for** $j = 1, \dots, M$ **do**

 (1) Partition $\Theta^{(l)}$, \mathbf{S} , $\Lambda^{(l)}$ and $\mathbf{V}^{(l)}$ as (26);

 (2) Draw $\gamma^{(l+1)} \sim \text{Gamma}\left(\frac{n}{2} + 1, \frac{s_{22} + (\lambda_{22}^{(l)})^2}{2}\right)$;

 (3) Draw $\beta^{(l+1)} \sim N_{M(p-1)}(-\mathbf{C}^{(l)} \bar{\mathbf{s}}_{21}, \mathbf{C}^{(l)})$, where $\mathbf{C}^{(l)} = ((\mathbf{D}_\tau^{(l)})^{-1} + (s_{22} + (\lambda_{22}^{(l)})^2)(\overline{\Theta_{11}^{-1}})^{(l)})^{-1}$;

 (4) Update

$\theta_{21}^{(l+1)} = (\beta^{(l+1)}, \mathbf{0})$, $\theta_{12}^{(l+1)} = \theta_{21}^{\mathbf{T}}$, $\theta_{22}^{(l+1)} = \gamma^{(l+1)} + (\beta^{(l+1)})^{\mathbf{T}} (\overline{\Theta_{11}^{-1}})^{(l+1)} \beta^{(l+1)}$

end

 2. Update $\Lambda^{(l)}$, i.e., draw sample

$(\lambda_{ij}^2)^{(l)} \sim \text{inverse Gamma}\left(\frac{M^2+1}{2}, \frac{1}{\nu_{ij}^{(l)}} + \frac{\|\Theta_{ij}^{(l+1)}\|_F^2}{2(\tau^2)^{(L)}}\right)$;

 3. Update $\mathbf{V}^{(l)}$, i.e., draw sample $\nu_{ij}^{(l)} \sim \text{inverse Gamma}\left(1, 1 + \frac{1}{(\lambda_{ij}^2)^{(l+1)}}\right)$;

 4. Update $\tau^{(l)}$ and $\zeta^{(l)}$, i.e.,

$(\tau^2)^{(l)} \sim \text{inverse Gamma}\left(\frac{M^2(p-1)p+2}{4}, \frac{1}{\zeta^{(l)}} + \sum_{i < j} \frac{\|(\Theta_{ij}^{(l+1)})\|_F^2}{2(\lambda_{ij}^2)^{(l+1)}}\right)$,

$\zeta^{(l)} \sim \text{inverse Gamma}\left(1, 1 + \frac{1}{(\tau^2)^{(l+1)}}\right)$;

end

 Store the sample precision matrix Θ ;

 Increment $l \leftarrow l + 1$.

end

Network 1, $p = 10$, dense data				Network 1, $p = 10$, $N = 100$		
	$N = 20$	$N = 100$	$N = 200$		Dense	Sparse
Bayes	0.65 (0.10)	0.88 (0.04)	0.94 (0.03)	Bayes	0.88 (0.04)	0.83 (0.04)
FGM	0.66 (0.06)	0.84 (0.03)	0.90 (0.03)	FGM	0.84 (0.03)	0.80 (0.04)

Network 1, $N = 100$, dense data				$p = 10$, $N = 100$, dense data		
	$p = 10$	$p = 30$	$p = 50$		Network 1	Network 2
Bayes	0.88 (0.04)	0.86 (0.02)	0.83 (0.02)	Bayes	0.88 (0.04)	0.91 (0.04)
FGM	0.84 (0.03)	0.84 (0.02)	0.85 (0.02)	FGM	0.84 (0.03)	0.92 (0.04)

Table 1: The mean area under the ROC curves for Bayesian fglasso and FGM. Standard errors are shown in parentheses.

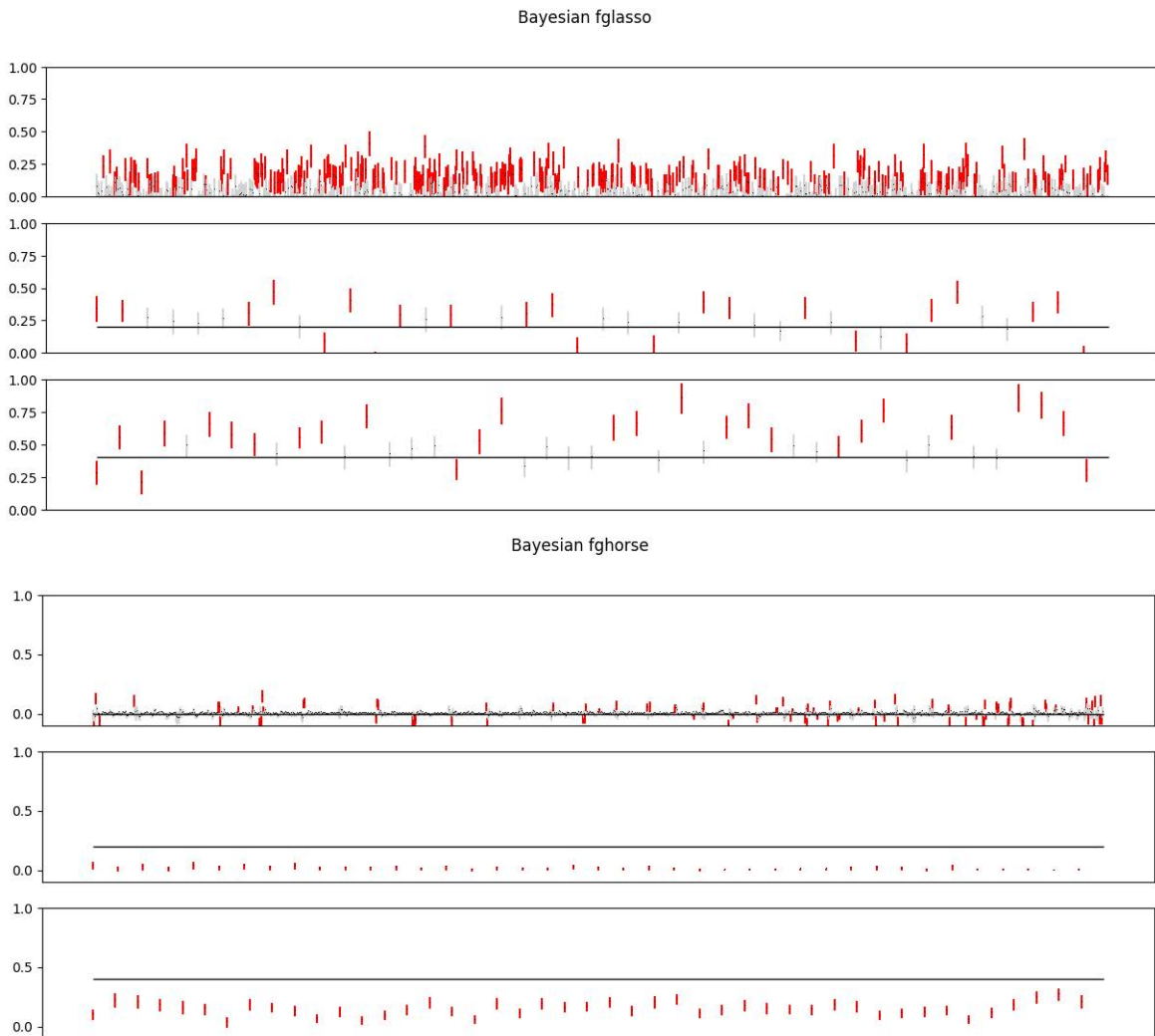


Figure 1: Posterior 50% equal-tailed credible intervals for off-diagonal elements θ_{ij} with weight 0, 0.2, and 0.4 (panels from top to bottom) for Bayesian fglasso and fghorse, separately. Red credible intervals are those that did not capture the true values. Black solid horizontal lines marked the true weights.

MSE				
	0 elements	0.2 elements	0.4 elements	Overall
fglasso	0.183 (0.001)	0.019 (0.006)	0.033 (0.009)	0.019 (0.002)
fghorse	0.001 (0.000)	0.032 (0.002)	0.051 (0.007)	0.004 (0.000)

Width of 50% CI				
	0 elements	0.2 elements	0.4 elements	Overall
fglasso	0.169 (0.003)	0.174 (0.004)	0.183 (0.004)	0.170 (0.003)
fghorse	0.034 (0.002)	0.044 (0.007)	0.099 (0.003)	0.037 (0.002)

Table 2: Summary of mean squared error (MSE), width of 50% credible intervals (Width) and bias based on 10 replications.

		Network 1			Network 2		
		p=10	p=30	p=50	p=10	p=30	p=50
fglasso	FPR (%)	6.07 (3.59)	0.95 (0.46)	13.87 (0.65)	8.61 (4.38)	1.13 (0.53)	16.06 (1.05)
	FNR (%)	38.82 (6.00)	62.46 (5.61)	32.27 (4.45)	24.44 (9.69)	50.00 (3.80)	27.78 (5.69)
	ERR (%)	18.44 (3.73)	9.01 (1.01)	15.33 (0.67)	11.78 (4.34)	4.16 (0.48)	16.41 (1.06)
	F 1	0.71 (0.06)	0.52 (0.06)	0.41 (0.02)	0.72(0.09)	0.60 (0.04)	0.21 (0.02)
	Sparsity (%)	26.89	5.75	18.14	22	4.16	17.71
fghorse	FPR (%)	18.57 (8.27)	2.14 (0.60)	1.03 (0.36)	10.83 (6.97)	0.74 (0.64)	0.40 (0.21)
	FNR (%)	22.35 (9.41)	36.14 (3.35)	41.81 (4.18)	24.44 (9.69)	41.11 (3.08)	43.06 (3.11)
	ERR (%)	20.00 (6.13)	6.60 (0.78)	4.26 (0.37)	13.56 (6.16)	3.24 (0.52)	1.66 (0.23)
	F 1	0.75(0.08)	0.72(0.03)	0.68(0.03)	0.70 (0.11)	0.69(0.03)	0.67(0.04)
	Sparsity (%)	40.89 (6.38)	10.23 (0.57)	5.56 (0.54)	23.78 (5.63)	4.34 (0.72)	2.07 (0.22)
FGM	FPR (%)	81.07 (10.11)	44.58 (4.48)	31.35 (4.08)	50.00 (16.76)	19.39 (6.44)	11.14 (2.22)
	FNR (%)	4.71 (6.86)	12.28 (2.48)	19.28 (4.68)	1.11 (3.33)	17.04 (5.79)	19.72 (5.19)
	ERR (%)	52.22 (5.28)	40.34 (3.85)	30.39 (3.44)	40.22 (13.42)	19.24 (5.87)	11.40 (2.10)
	F 1	0.58 (0.03)	0.36 (0.02)	0.30 (0.02)	0.51 (0.09)	0.36 (0.06)	0.30 (0.04)
	Sparsity (%)	86.44	50.23	35.26	59.78	23.33	13.18
True sparsity (%)		37.78	13.1	7.92	20	6.21	2.94

Table 3: Summary statistics of false positive (FPR), false positive rate (FNR), misclassification rate (ERR), F1 (Dice) score and estimated graph sparsity of graph estimation with 10 data sets generated by dense functional data with underground Network 1 and 2 separately. “fglasso” refers to the Bayesian functional graphical lasso method with gamma prior for shrinkage parameter λ ; “fghorse” refers to the functional graphical horseshoe method, while “FGM” refers to the frequentist version of functional graphical lasso model proposed by Qiao et al. (2019). The means are reported here, the standard errors are shown in parentheses.

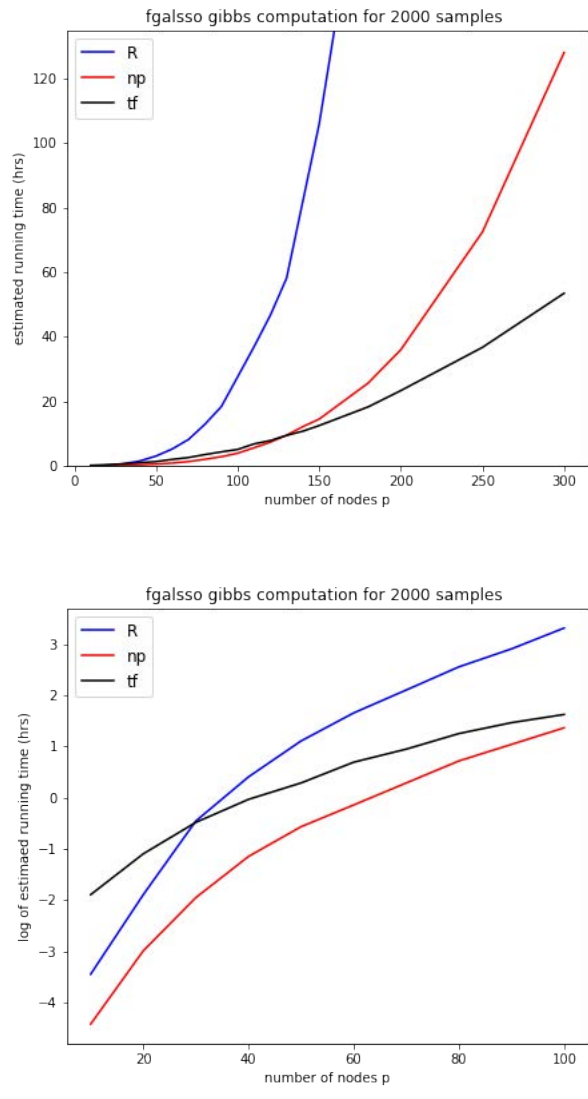


Figure 2: Computational cost as a function of p for the block Gibbs sampler under three environments, **R** (R), **NumPy** (np), **Tensorflow** (tf). Estimated wall time (left) and its logarithm (right) versus number of nodes p . Note the difference in the range of p in the left and right plots, and the change in ranking at lower numbers of nodes versus higher numbers.

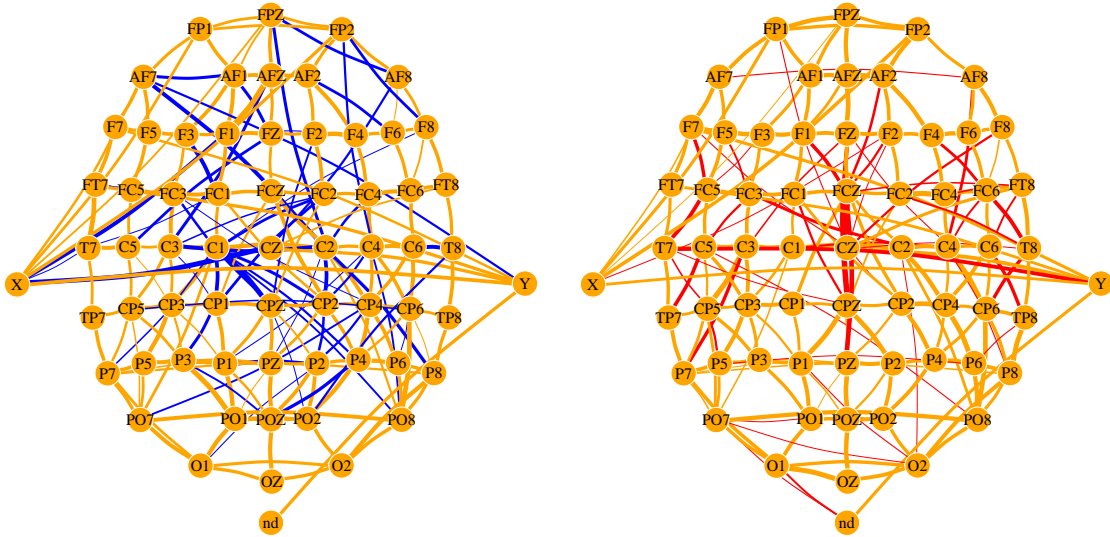


Figure 3: The estimated networks for the alcoholic group (left) and control group (right) from the EEG study. The thickness of edges indicates the weights. Blue lines denote edges identified only in the alcoholic group, red denote edges identified only in the control group, and orange denote edges identified both in alcoholic and control groups.

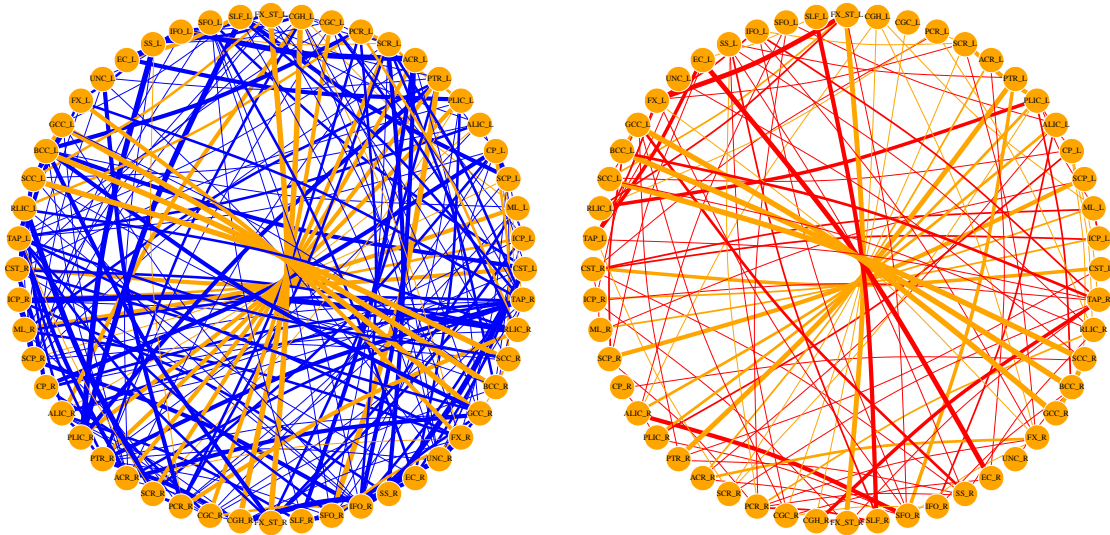


Figure 4: The estimated weighted brain connectivity graphs for TBI (left) and control (right) groups. Nodes names are marked with abbreviation of ROIs, which are defined in Table 4. The thicker edges indicate larger weights; Blue lines denote edges identified only by the TBI group, red denote edges identified only by the control group, and orange denote edges identified by both groups.

Label	Hemisphere	ROI
CST	left, right	Corticospinal tract
ICP	left, right	Inferior cerebellar peduncle
ML	left, right	Medial lemniscus
SCP	left, right	Superior cerebellar peduncle
CP	left, right	Cerebral peduncle
ALIC	left, right	Anterior limb of internal capsule
PLIC	left, right	Posterior limb of internal capsule
PTR	left, right	Posterior thalamic radiation, includes optic radiatio
ACR	left, right	Anterior corona radiata
SCR	left, right	Superior corona radiata
PCR	left, right	Posterior corona radiata
CGC	left, right	Cingulum, cingulate gyrus
CGH	left, right	Cingulum (hippocampus), cingulate gyrus
FX.ST	left, right	Fornix (cres) / Stria terminalis
SLF	left, right	Superior longitudinal fasciculus
SFO	left, right	Superior fronto-occipital fasciculus, could be a part of anterior internal capsule
IFO	left, right	Inferior fronto-occipital fasciculus
SS	left, right	Sagittal stratum, includes inferior longitudinal fasciculus and inferior fronto-occipital fasciculus
EC	left, right	External capsule
UNC	left, right	Uncinate fasciculus
FX	left, right	Fornix, column and body of fornix
GCC	left, right	Genu of corpus callosum
BCC	left, right	Body of corpus callosum
SCC	left, right	Splenium of corpus callosum
RLIC	left, right	Retrolenticular part of internal capsule
TAP	left, right	Tapatum

Table 4: Index of the “Eve” white matter atlas labels corresponding to Figure 4 the TBI connectivity study.